Nitroarylurea-terminated supramolecular polymers that exhibit facile thermal repair and aqueous swelling-induced sealing of defects

Article

Supplemental Material

Baker, B. C., German, I. M., Chippindale, A. M. ORCID: https://orcid.org/0000-0002-5918-8701, Mcewan, C. E. A., Stevens, G. C., Colquhoun, H. M. and Hayes, W. ORCID: https://orcid.org/0000-0003-0047-2991 (2018) Nitroarylurea-terminated supramolecular polymers that exhibit facile thermal repair and aqueous swelling-induced sealing of defects. Polymer, 140. pp. 1-9. ISSN 0032-3861 doi: 10.1016/j.polymer.2018.02.029 Available at https://centaur.reading.ac.uk/75554/

To link to this article DOI: http://dx.doi.org/10.1016/j.polymer.2018.02.029

Publisher: Elsevier

Nitroarylurea-terminated supramolecular polymers that exhibit facile thermal repair and swelling-induced sealing of defects

Supplementary Information

Benjamin C. Baker[a]; *Ian M. German*[b]; *Ann M. Chippindale*[a]; *Corinne E. A. McEwan*[a]; *Gary C. Stevens*[b]; *Howard M. Colquhoun*[a]; *and Wayne Hayes*[a]*

[a] Department of Chemistry, University of Reading, Whiteknights, Reading, RG6 6AD, UK. Email: w.c.hayes@reading.ac.uk, Telephone: +44 118 378 6491, Fax: +44 118 378 6331

[b] Gnosys Global Ltd., 17-18 Frederick Sanger Road, The Surrey Research Park, Guildford, Surrey, GU2 7YD, UK

Contents

Scheme S1; Synthetic route to molecule **1**. 3

Scheme S2; Synthetic route to molecules **2** and **3.** 3

Figures S1-8; ^{1}H and ^{13}C NMR spectra of **1-6** DMSO-d_6. 4-11

Figures S9-16; IR spectra of **1-6**. 12-15

Figure S17; Computer simulation (molecular mechanics) of a low molecular weight gelator derivative of **1**. 16

Figure S18; Crystal structure analysis of end group 1-(4-aminophenyl)-3-(3-nitrophenyl)urea (**7**). 17

Table S1; Crystallographic data for 1-(4-aminophenyl)-3-(3-nitrophenyl)urea (**7**). 18

Figure S19; Plot of ^{1}H NMR chemical shift of amide NH protons vs. concentration of **1** in $CDCl_3$. 19

Figure S20; ^{1}H NMR dilution studies of **1** in $CDCl_3$ where the concentration ranges from 14.0 mM to 2.6 mM. 19

Figures S21-24; Vertically placed glass slide flow studies of **1-6**. 20-21

Figures S25-26; DSC scans for **1** blended with **2** and **3**. 22

Figures S27-30; Microscopic images for healing of casts of **1-3**. 23-24

Figure S31; Film of 1/3 (1:1 % wt) where; A) pristine cast film, B) damage initiated with scapula, C) slide after 20 minutes, D) healed sample after 40 minutes 25

Figure S32-34; Plot of percentage weight loss monitored via TGA of **1**, **3** and system of **1/3** (1:1 % wt.) 25-26

Figures S35; Images of puncture closure system via swelling. 27

Figures S36-38; Plots of flow rate of water against time for puncture closure via swelling of casts of **1**, **3** and **1/3** (1:1 by wt.). 27-28

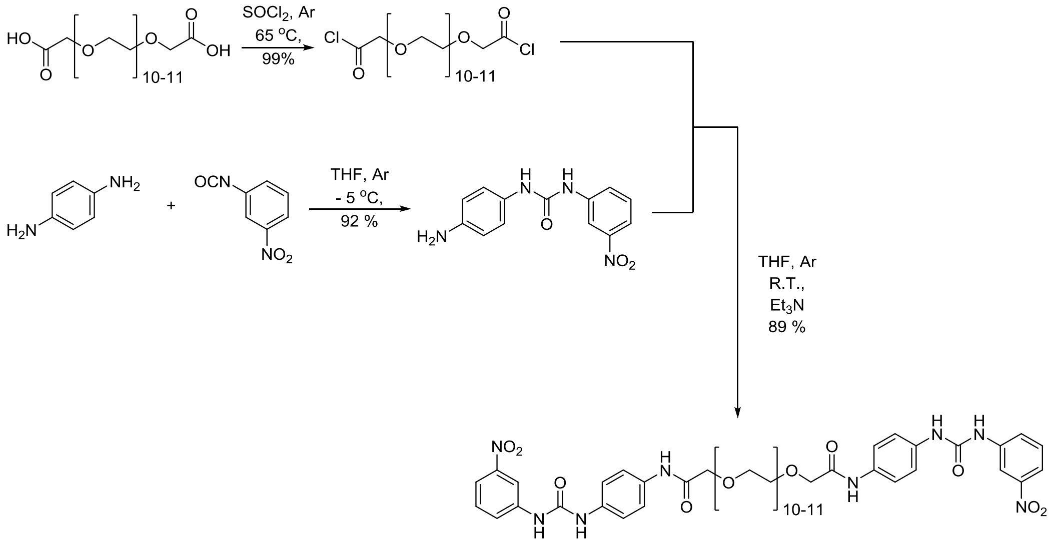

Scheme S1. Synthetic route to bisfunctionalised PEG **1**.

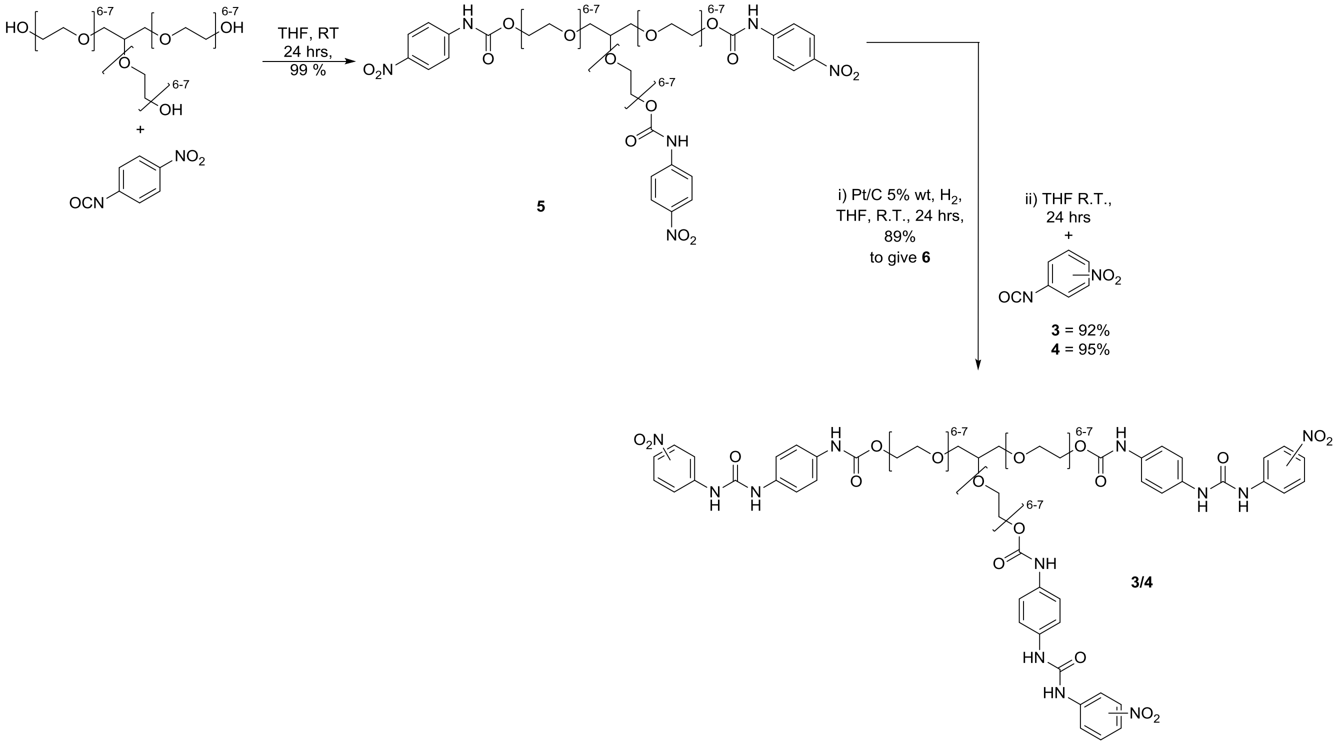

Scheme S2. Synthetic route to trisfunctionalised PEGS with the terminal nitro moieties in the *meta* (**2**) or *para* (**3**) position.

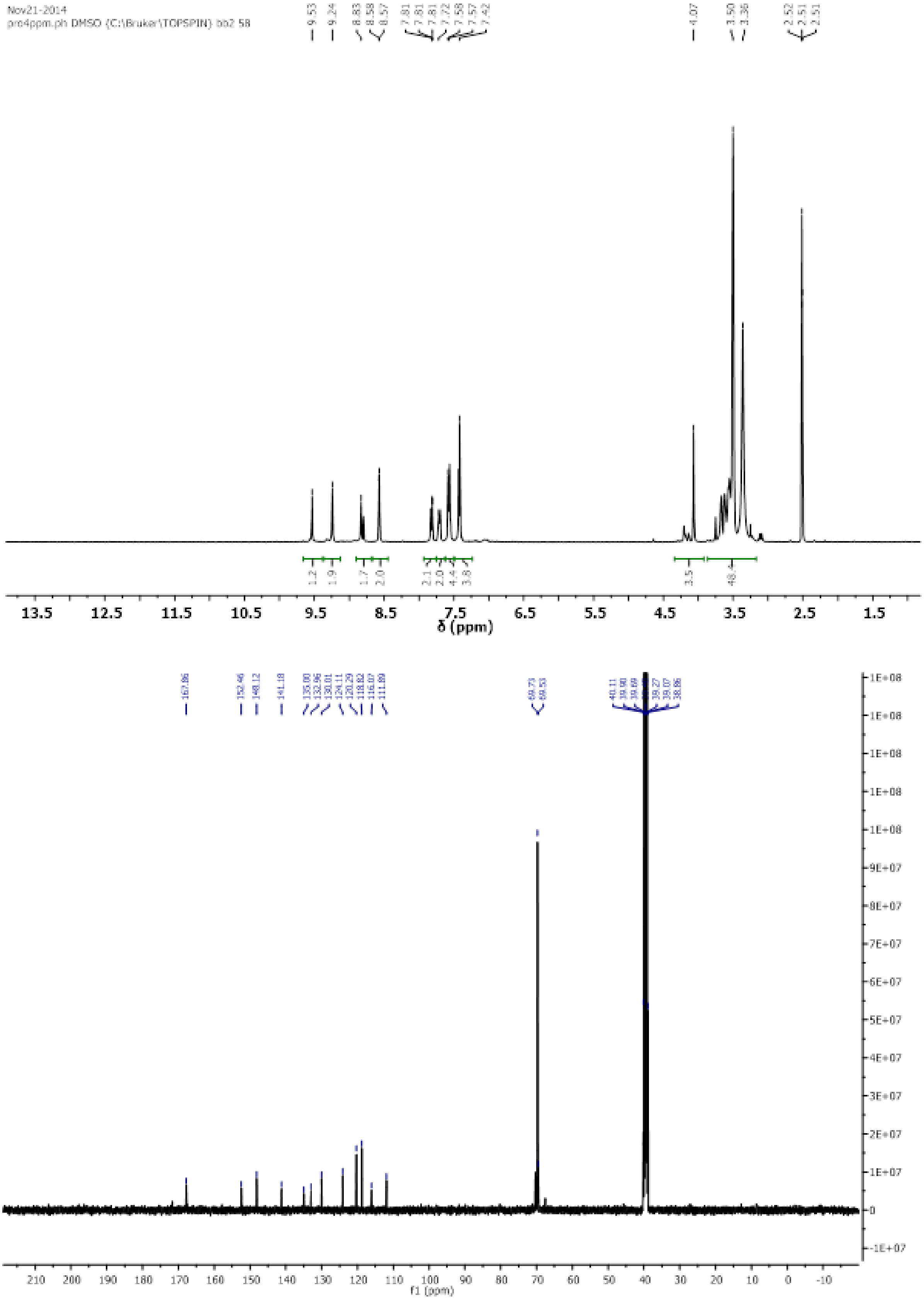

Figure S1. ^{1}H and ^{13}C NMR spectra of **1** in DMSO-d_6

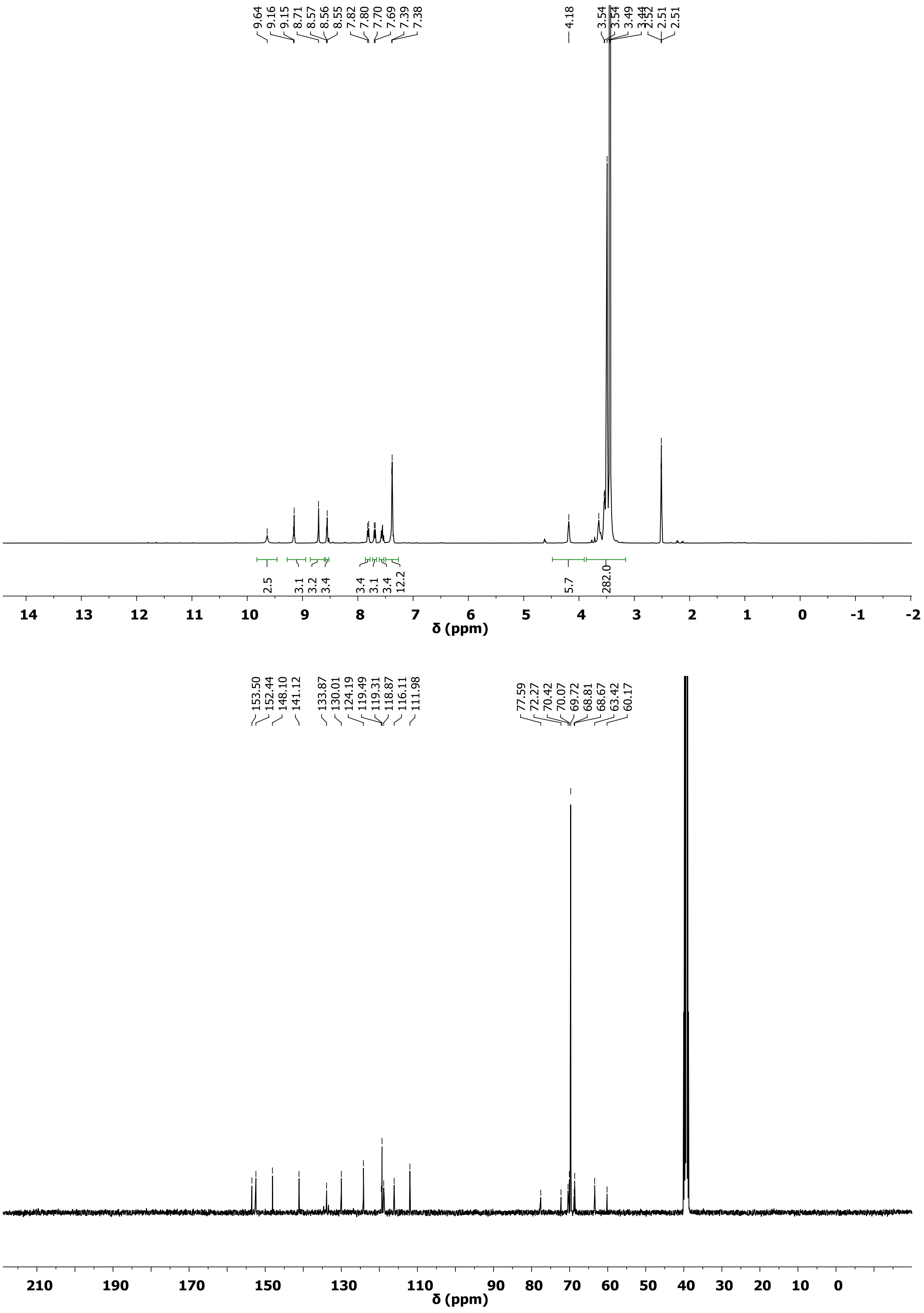

Figure S2. ^{1}H and ^{13}C NMR spectra of **2** in DMSO-*d*$_6$

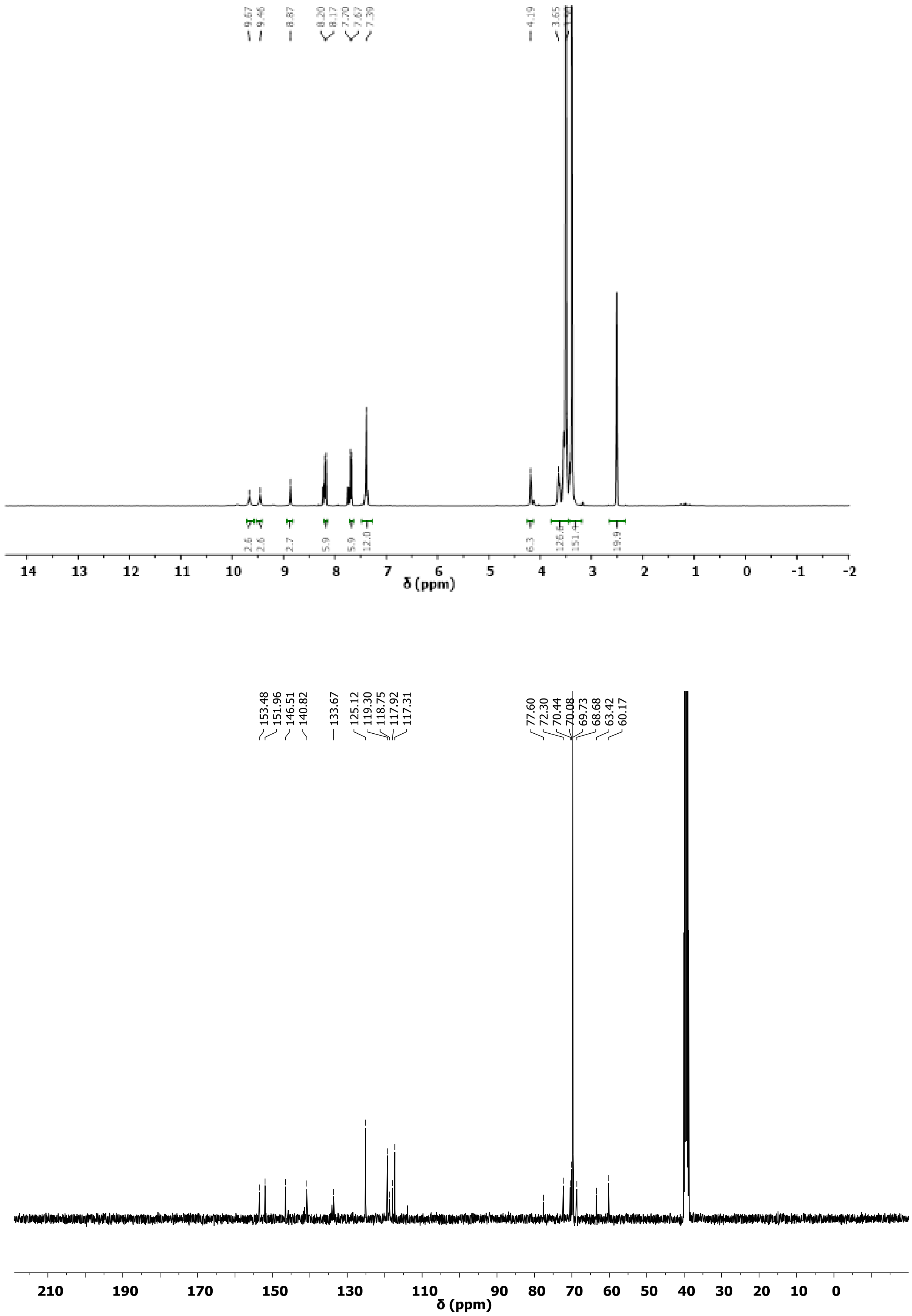

Figure S3. ^{1}H and ^{13}C NMR spectra in **3** DMSO-*d*$_6$

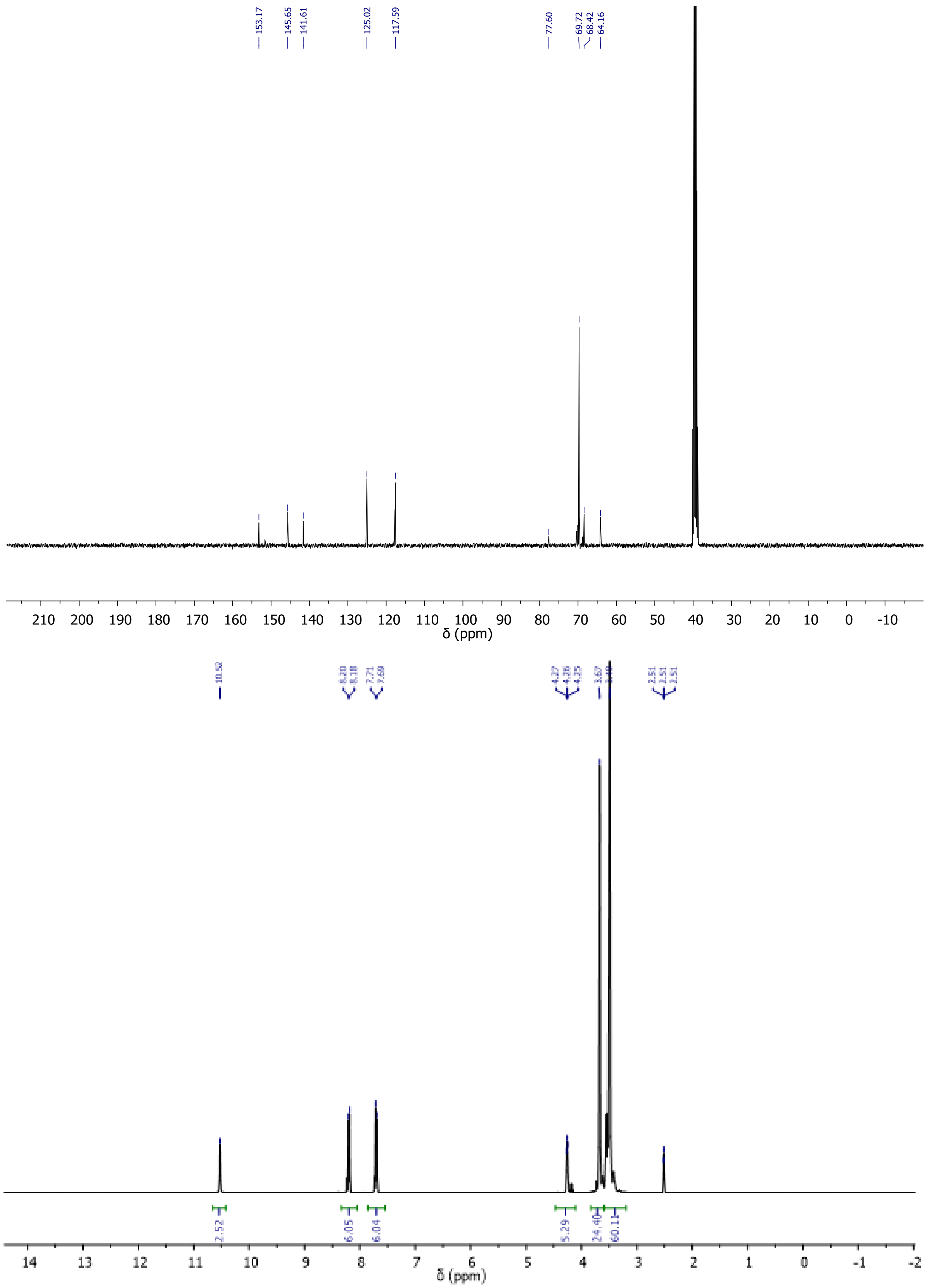

Figure S4. ^{1}H and ^{13}C NMR spectra of tris(4-nitrophenyl carbamato)glycerol ethoxylate (precursor to **2/3)** in DMSO-d_6

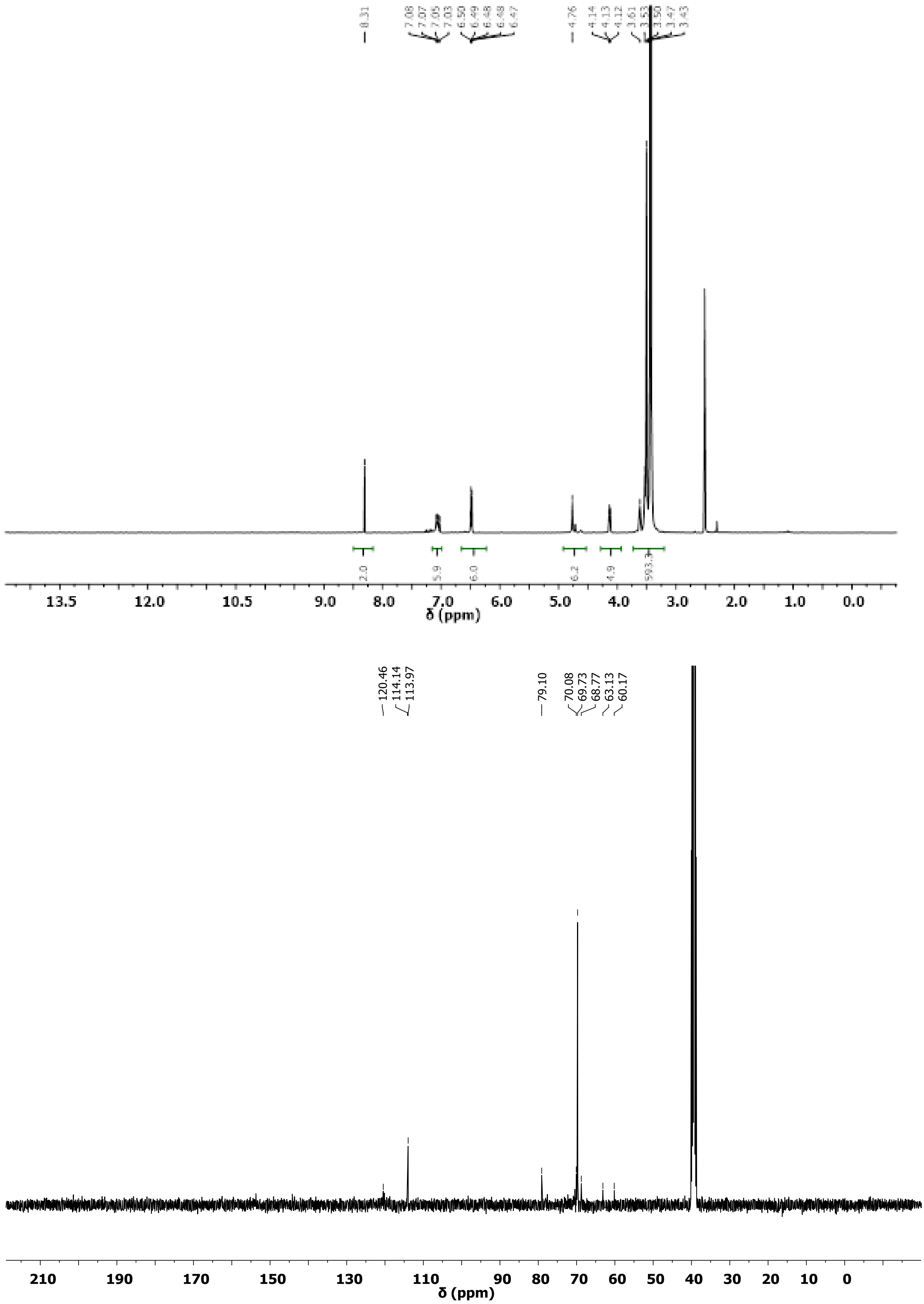

Figure S5. ^{1}H and ^{13}C NMR spectra of tris[(4-aminophenyl)-3-(3-nitrophenyl)urea]glycerol ethoxylate (precursor to **2/3)** in DMSO-d_6

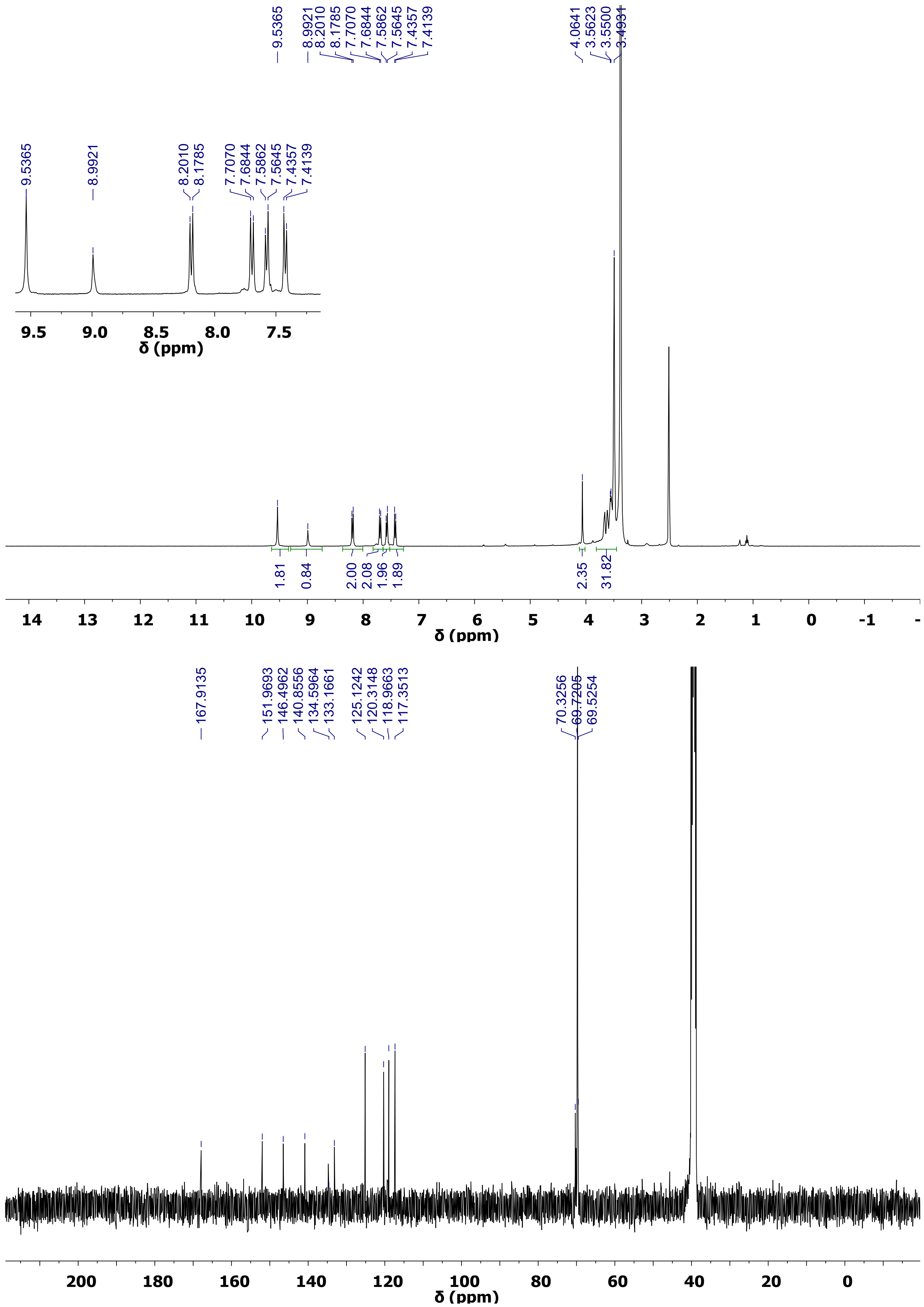

Figure S6. ^{1}H and ^{13}C NMR spectra of **4** in DMSO-d_6

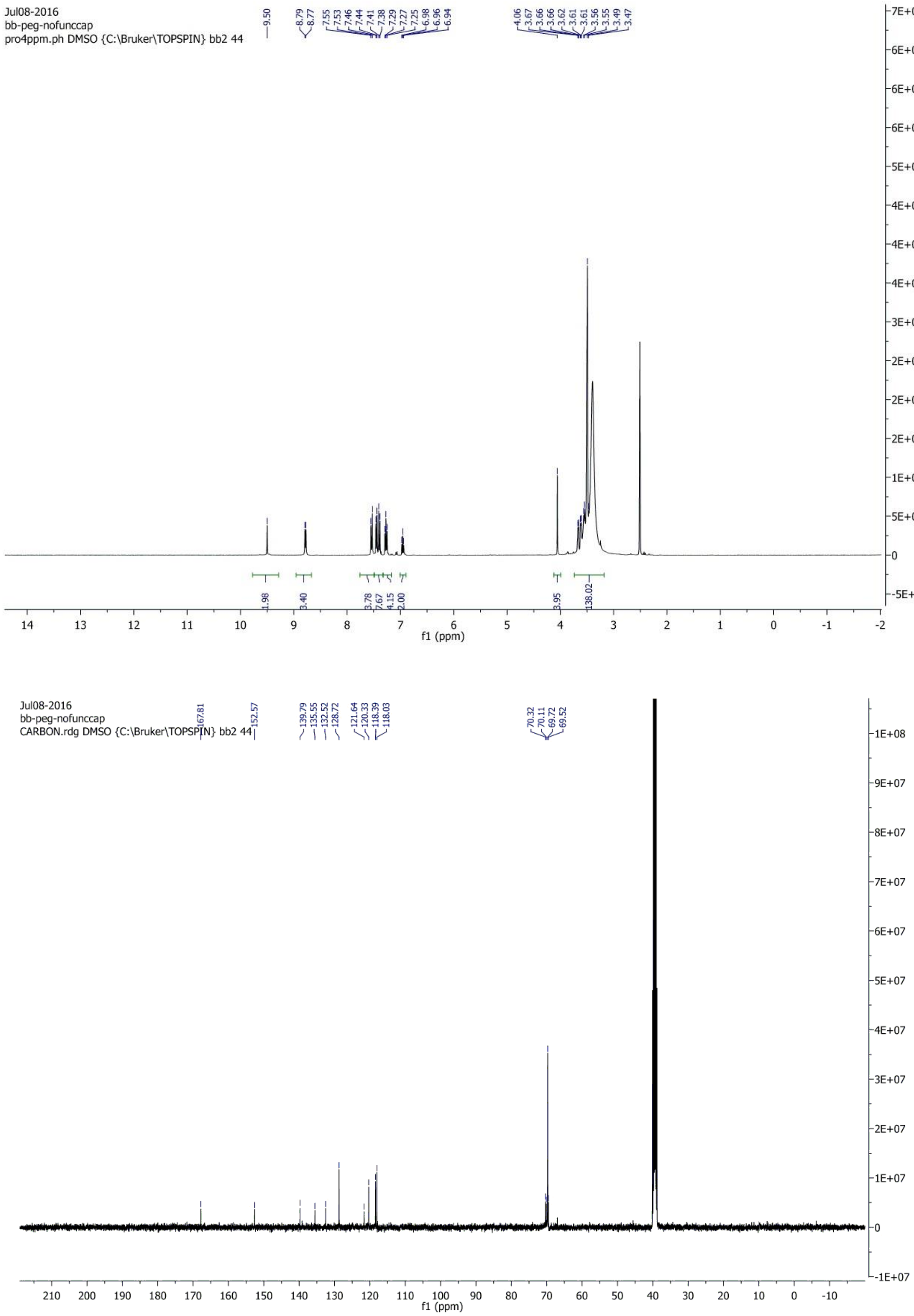

Figure S7. ^{1}H and ^{13}C NMR spectra of **5** in DMSO-d_6

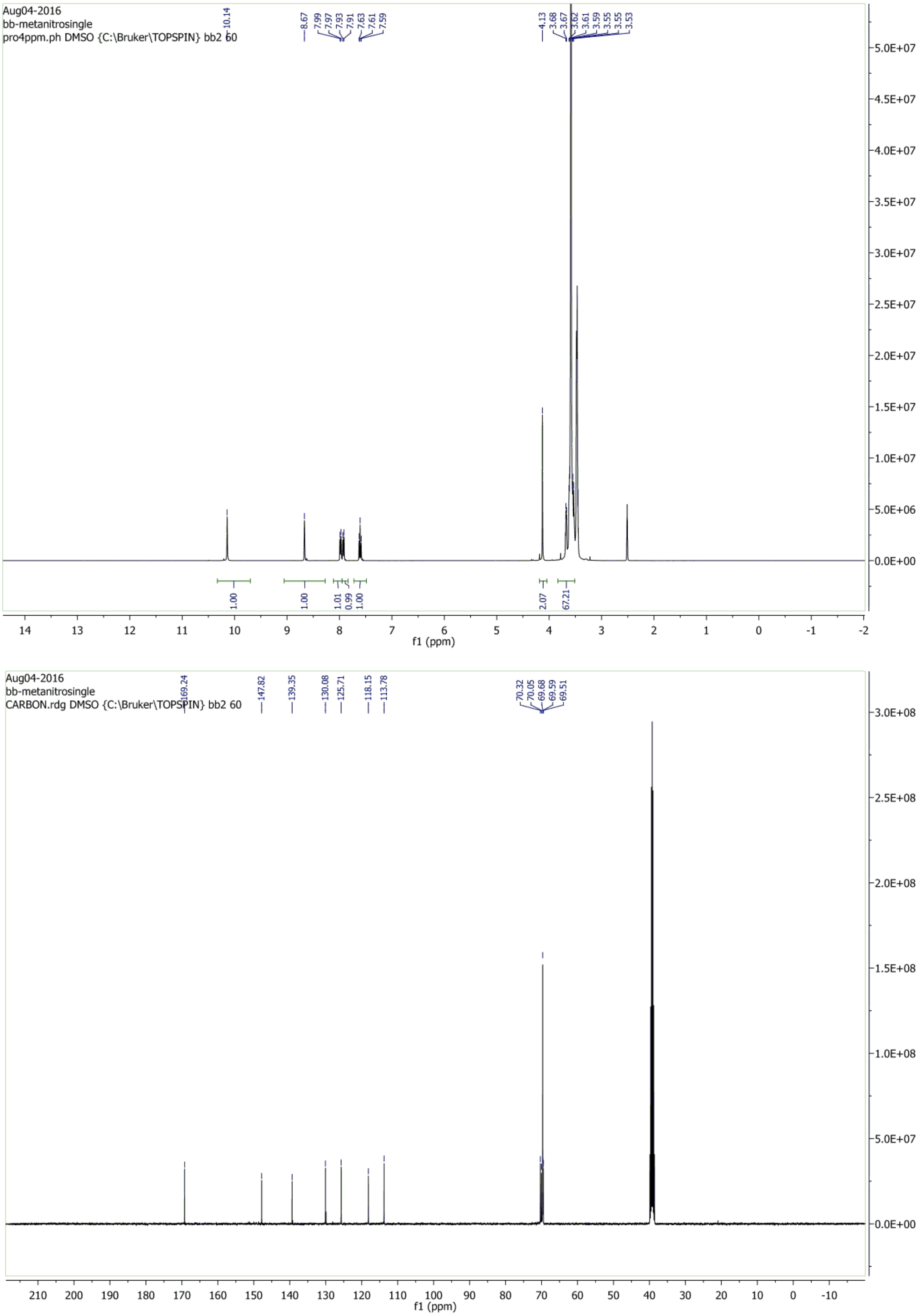

Figure S8. ^{1}H and ^{13}C NMR spectra of **6** in DMSO-*d*$_6$

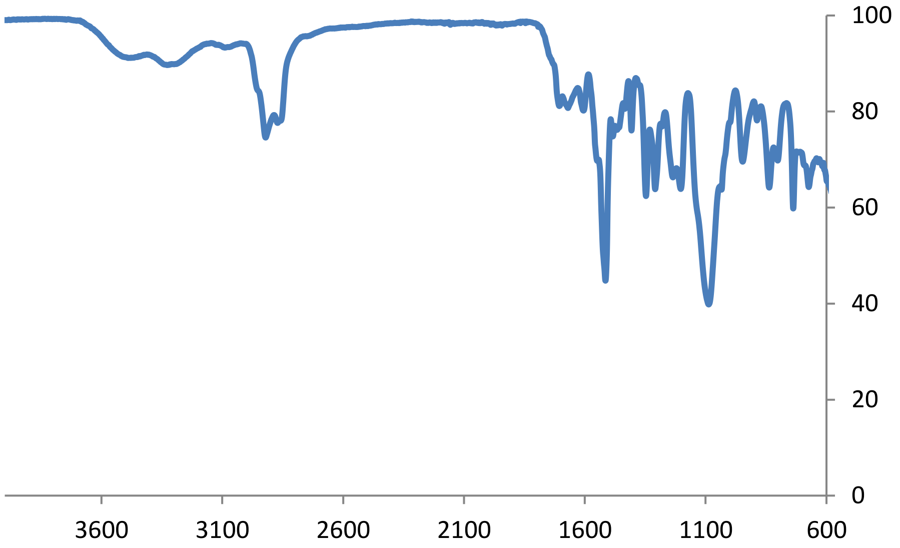

Figure S9. IR spectrum of **1**

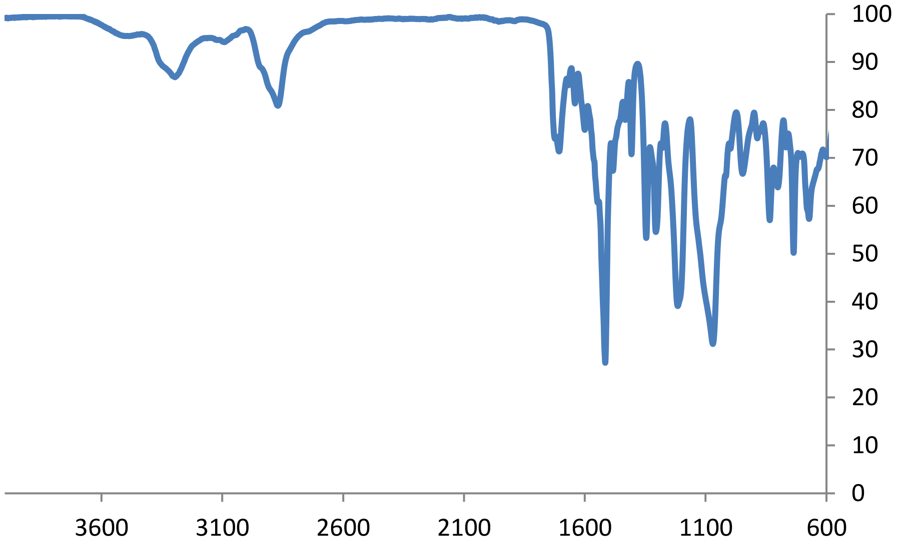

Figure S10. IR spectrum of **2**

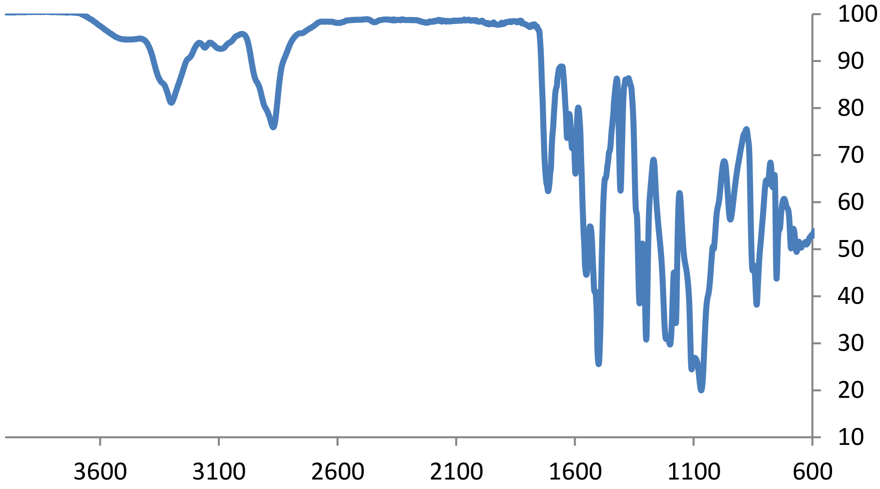

Figure S11. IR spectrum of **3**

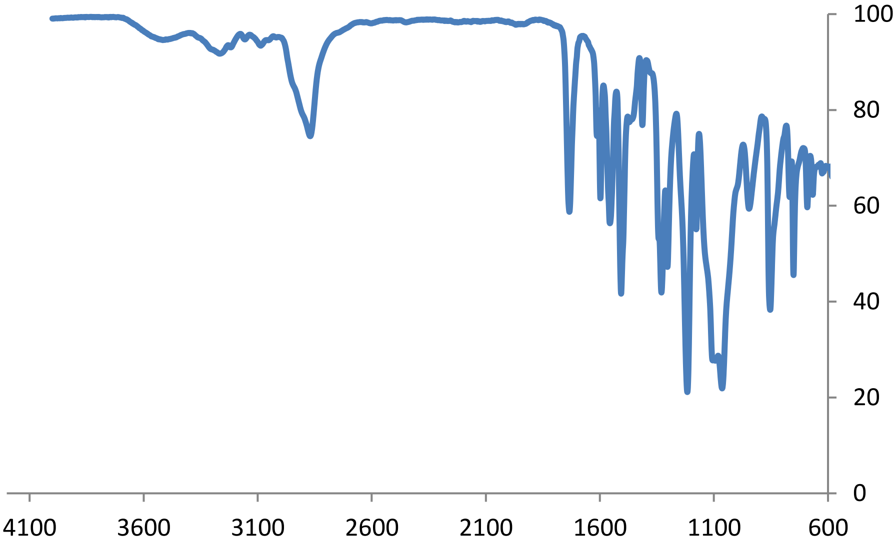

Figure S12. IR spectrum of tris(4-nitro phenyl carbamato)glycerol ethoxylate (precursor to **2/3)**

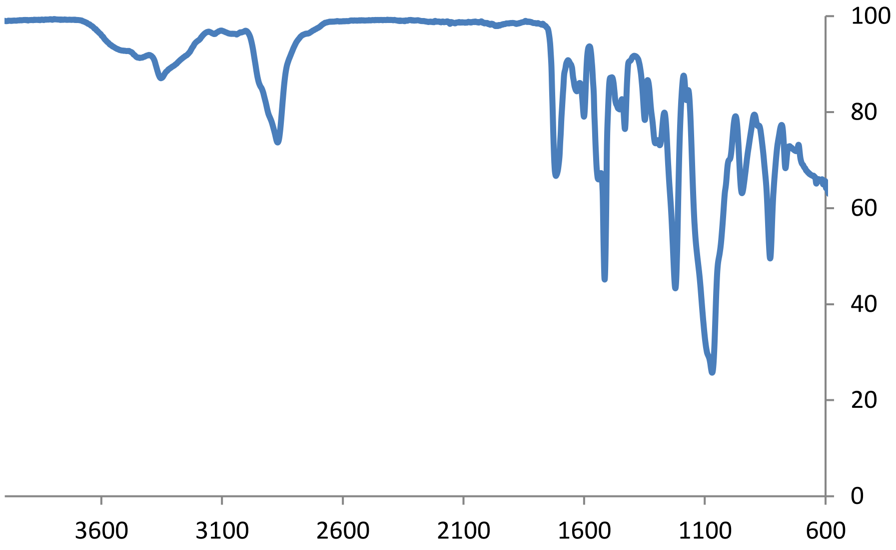

Figure S13. IR spectrum of tris[(4-aminophenyl)-3-(3-nitrophenyl)urea]glycerol ethoxylate (precursor to **2/3)**

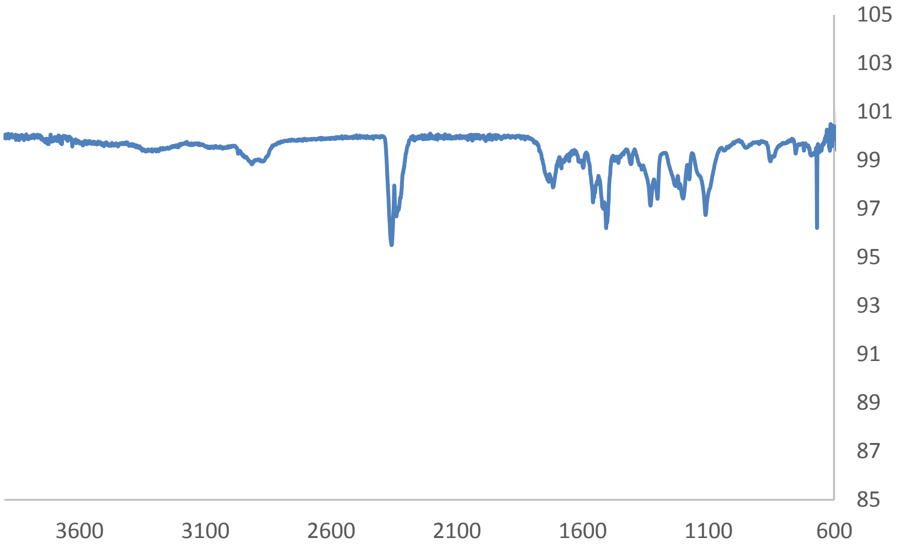

Figure S14. IR spectrum of **4**

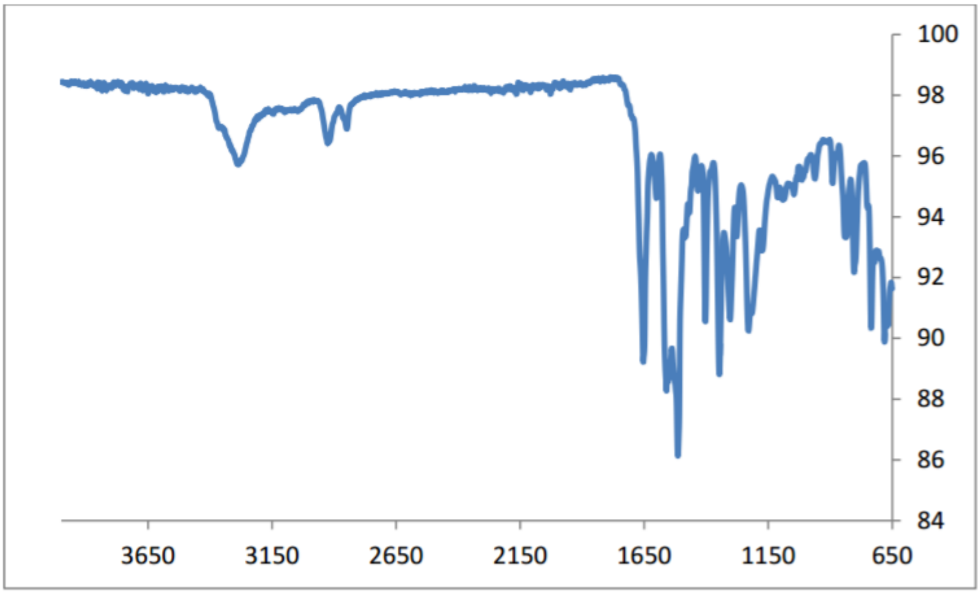

Figure S15. IR spectrum of **5**

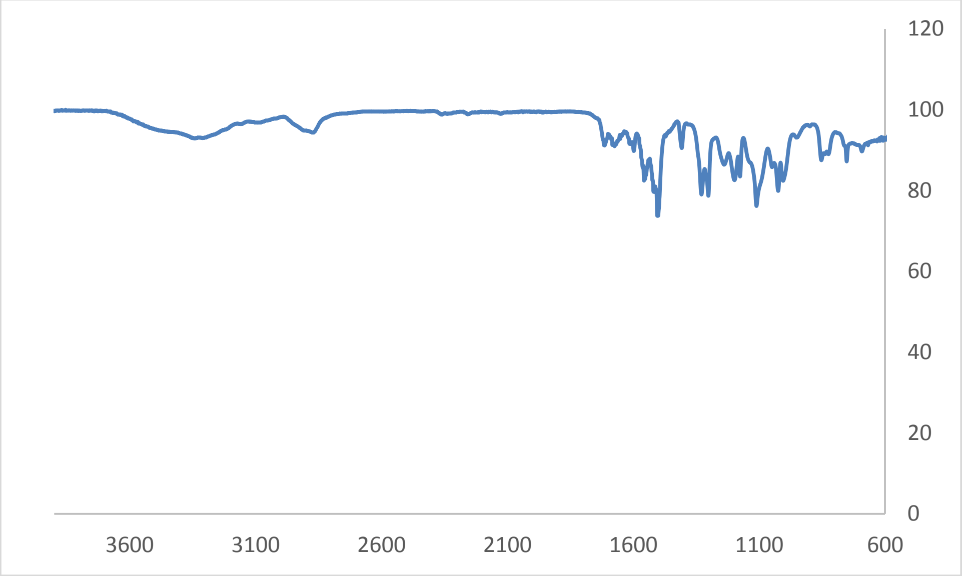

Figure S16. IR spectrum of **6**

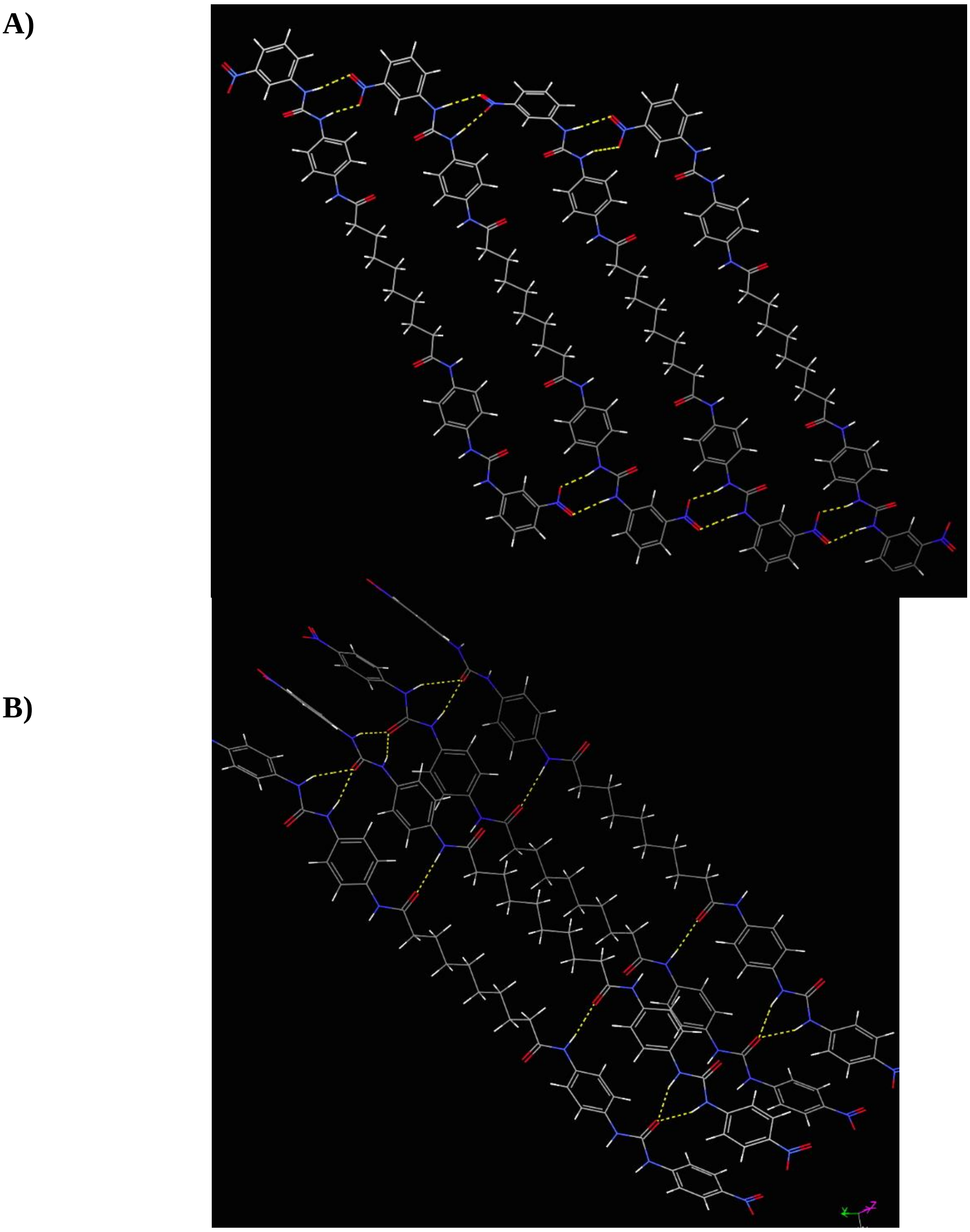

Figure S17. Computational simulation (molecular mechanics) of the interactions between A) bisaromatic nitro gelator, showing the one dimensional growth caused by hydrogen bond formation between the urea groups and the *meta*-nitro groups desirable for gelation, and B) *para*-nitro analogue of the gelator shown in A.

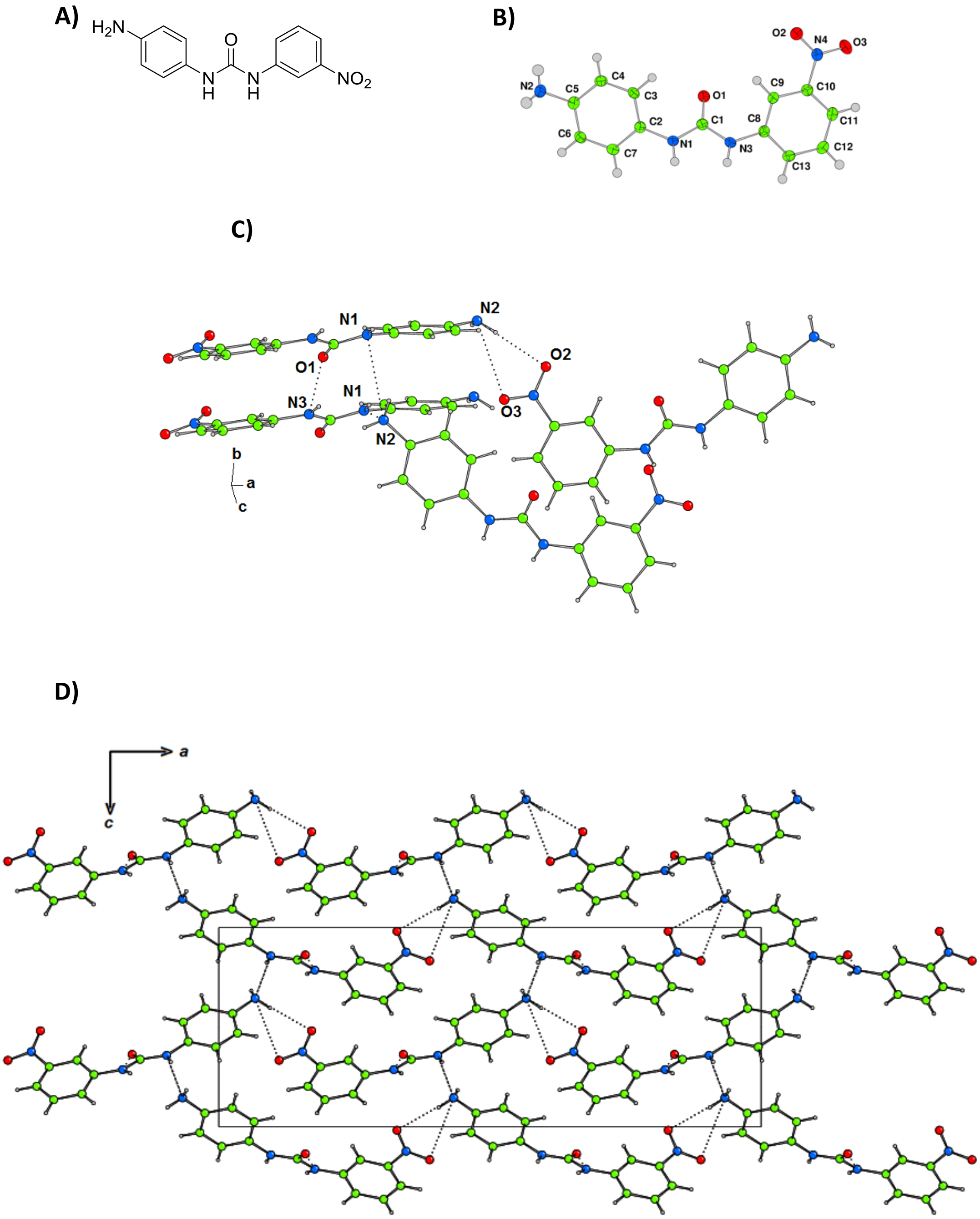

Figure S18. Crystal structure of 1-(4-aminophenyl)-3-(3-nitrophenyl)urea (**7**): a model compound for the end group **A)** molecular formular of (1-(4-aminophenyl)-3-(3-nitrophenyl)urea); **B)** asymmetric unit and numbering scheme; **C)** view showing hydrogen bonds between the meta-nitro groups and the aniline units of **7**; **D)** extended crystal structure of end groups viewed along the *b* axis

Table S1. Crystallographic data for 1-(4-aminophenyl)-3-(3-nitrophenyl)urea **(7)**

Formula	$C_{13}\,H_{12}\,N_4\,O_3$
M_r	272.27
Crystal system	orthorhombic
Space group	$P\ c\ a\ 2_1$
Z	4
a /Å	26.0654(8)
b/Å	4.86749(15)
c /Å	9.5612(2)
V / Å^3	1213.06(6)
D_{calc} / g cm^{-3}	1.491
Crystal habit	colourless plate
Crystal dimensions /mm	0.01 × 0.04 × 0.07
Radiation	Mo K_α (0.71073 Å)
T /K	150
μ /mm^{-1}	0.917
$R(F)$, $Rw(F)$	2.680, 3.096
CCDC cif deposition number	1456760

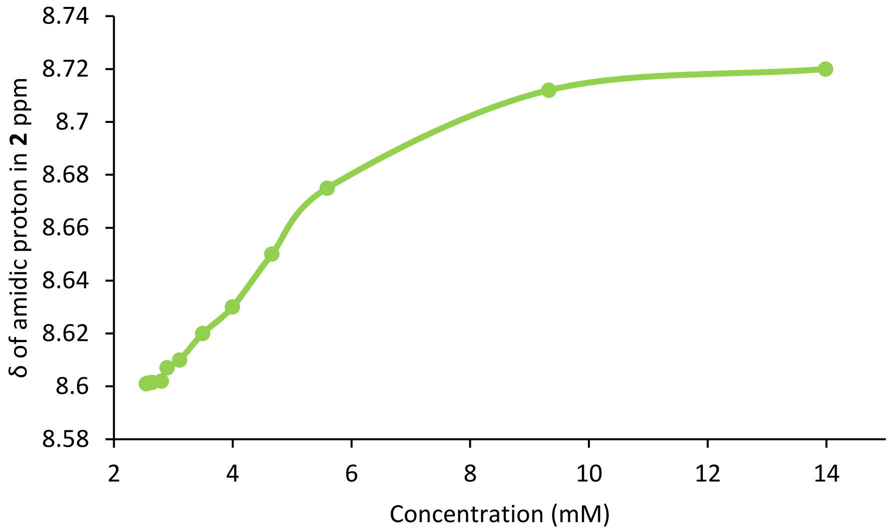

Figure S19. Plot of ^{1}H NMR chemical shift of amide NH protons *vs*. concentration of **1** in $CDCl_3$.

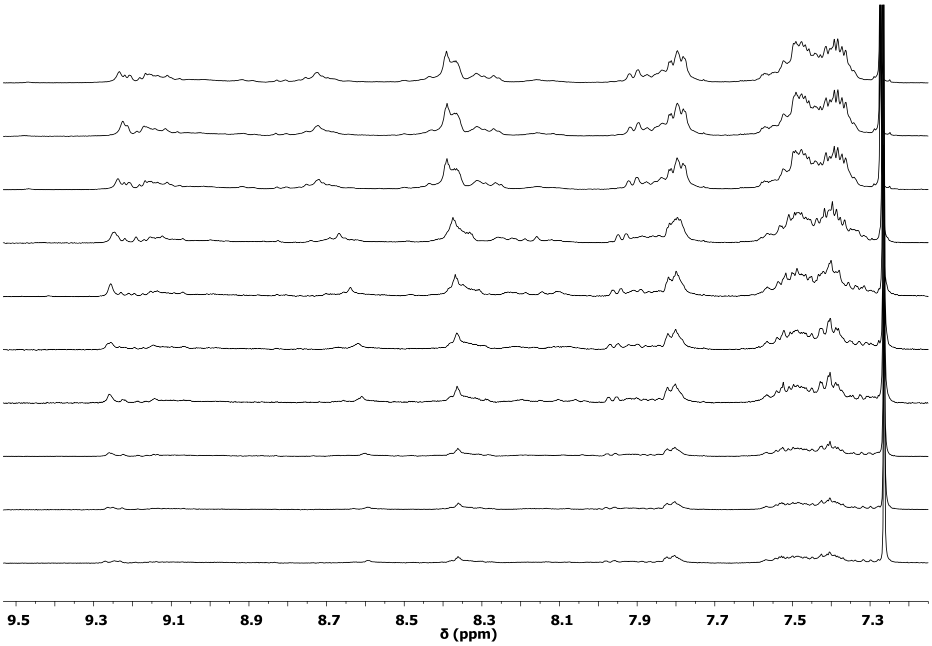

Figure S20. ^{1}H NMR dilution studies of **1** in $CDCl_3$ where the concentration ranges from 14.0 mM (top spectrum) to 2.6 mM (bottom spectrum).

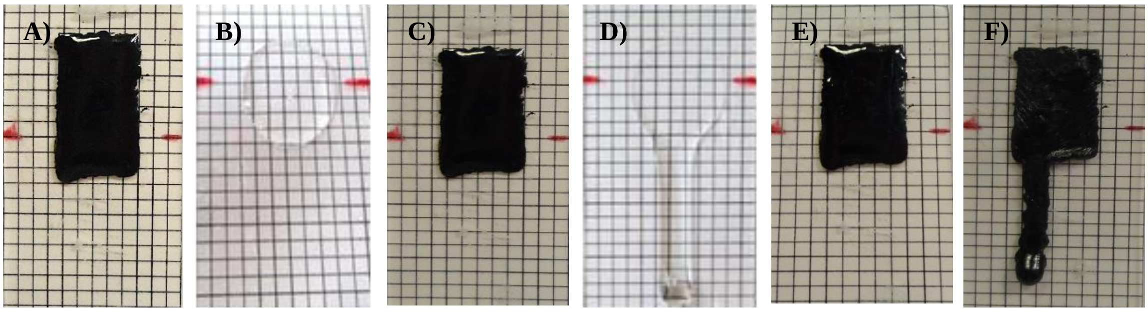

Figure S21. Vertically placed films where; A) **1** at time zero, B) unfunctionalised PEG 600 at time zero, C) **1** at 10 minutes, D) unfunctionalised PEG 600 at 10 minutes, E) **1** at 4 months at 25 °C, F) **1** at 72 hours at 35 °C, on 1 × 1 mm grid backing paper (average film dimensions 5 × 9 × 1 mm)

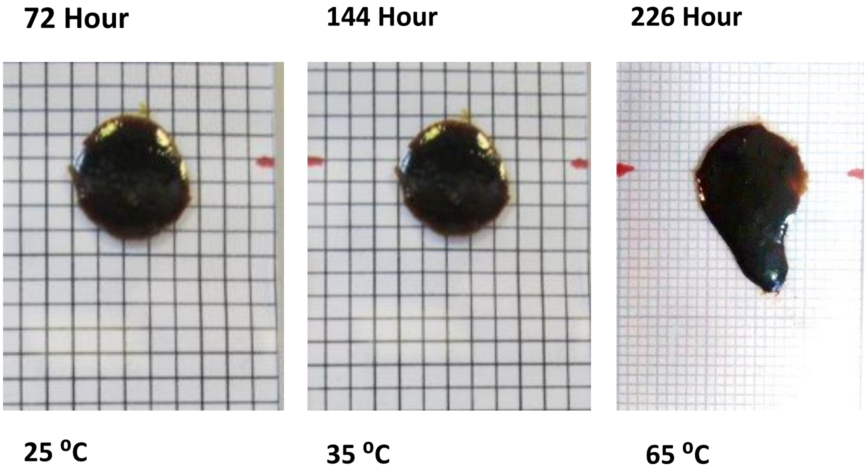

Figure S22. Vertically placed blended film of **1** and **2** (at 1:1 % wt) after 72 hours at 25 °C, 72 hours at35 °C and 72 hours at 65 °C. The backing paper grid in the two left images is 1 × 1 mm whereas for the right hand image it is 0.5 × 0.5 mm (average film dimensions 5 × 1 mm).

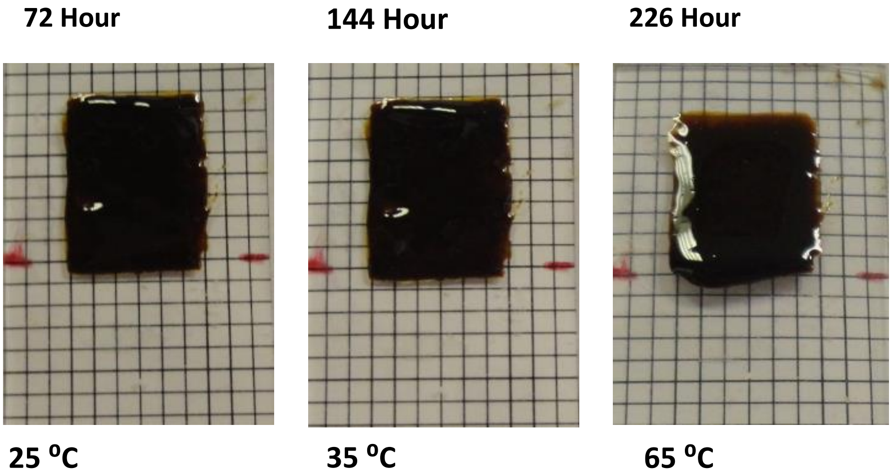

Figure S23. Films of **1/3** (1:1 % wt) after 72 hours at 25 °C, 72 hours at 35 °C and 72 hours at 65 °C. The backing paper grid for these images is 1 × 1 mm.

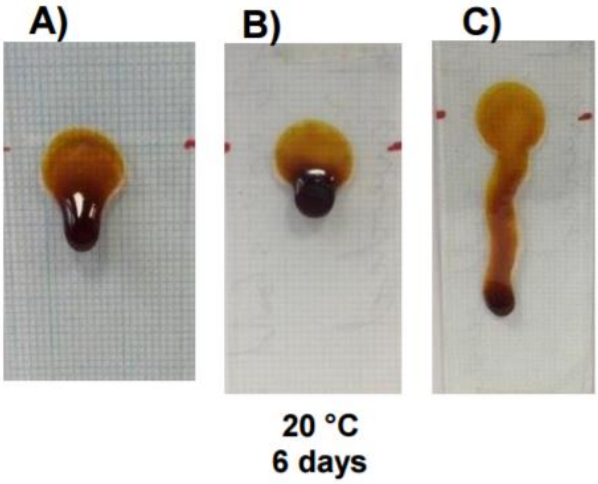

Figure S24. Vertically placed film casts of A) **4**, B) **5**, C) **6** after 6 days at 20 °C after casting as a circle. The backing paper grid is 0.5 × 0.5 mm (average film dimensions 5 × 1 mm).

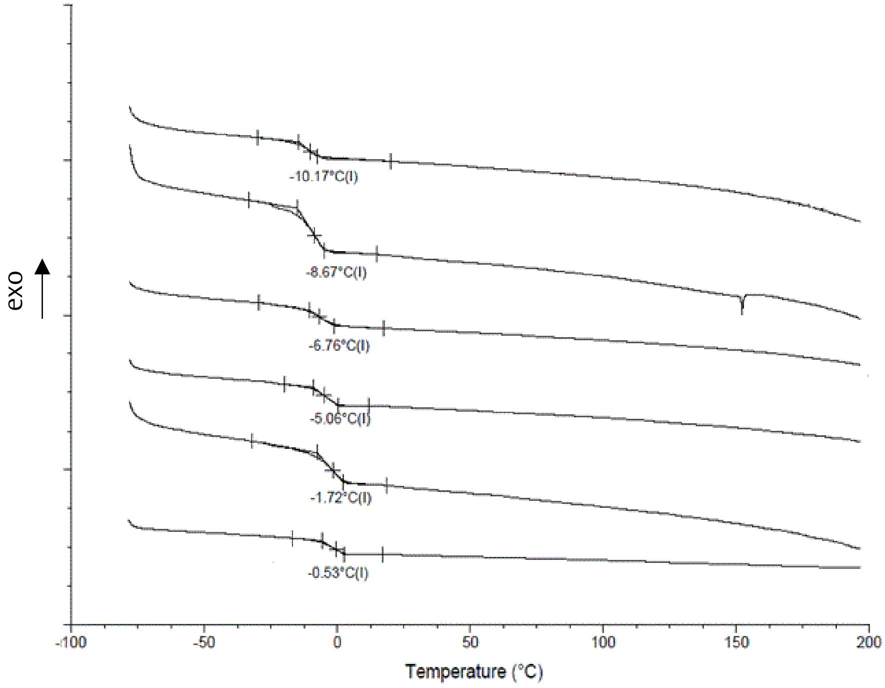

Figure S25. DSC heating curves (second scan) for samples of **1** (top) and blends of **1/2** where the percentage weight of **3** is; 25, 50, 60, 80, 100 (bottom) and heating rate is 10 °C/min. T_gs are shown as midpoints.

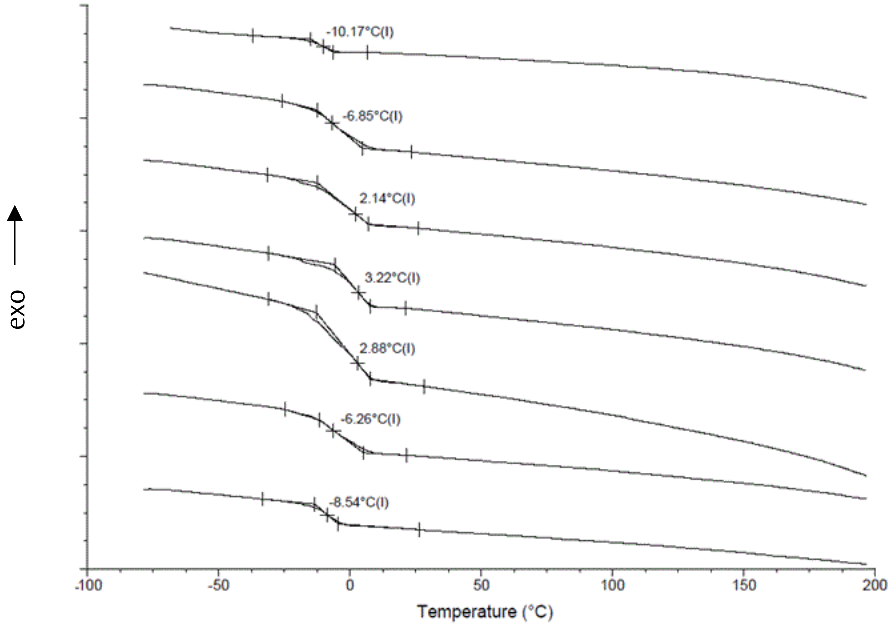

Figure S26. DSC heating curves (second scan) for samples of **1** (top) and blends of **1/3** where the percentage weight of **4** is; 15, 40, 50, 65, 85, 100 (bottom) and heating rate is 10 °C/min. T_gs are shown as midpoints.

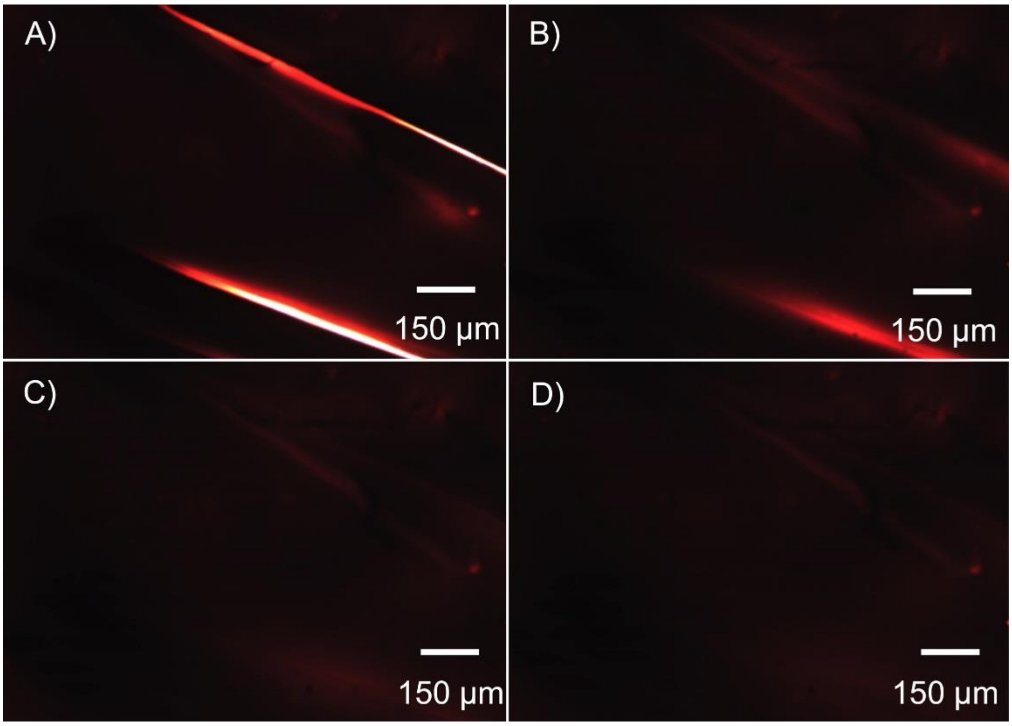

Figure S27. Optical micrographs of film of **1** after defect formation where; A) 0 minutes, B) 10 minutes, C), 20 minutes D) 60 minutes (20 °C) (film thickness = 1 mm).

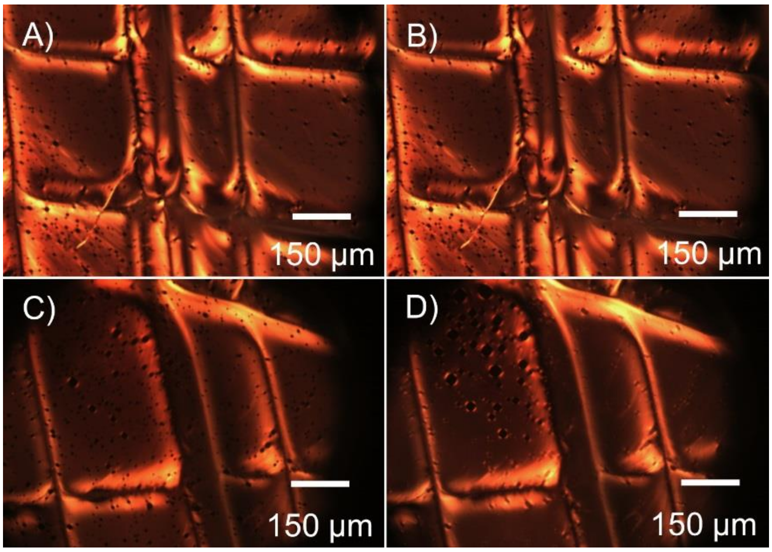

Figure S28. Optical micrographs of film of **2** after defect formation where; A) 0 minutes (20 °C), B) 60 minutes (20 °C), C) heated to 100 °C, D) heated to 200 °C after defect formation, (heating rate 2 °C /min) (film thickness = 1 mm).

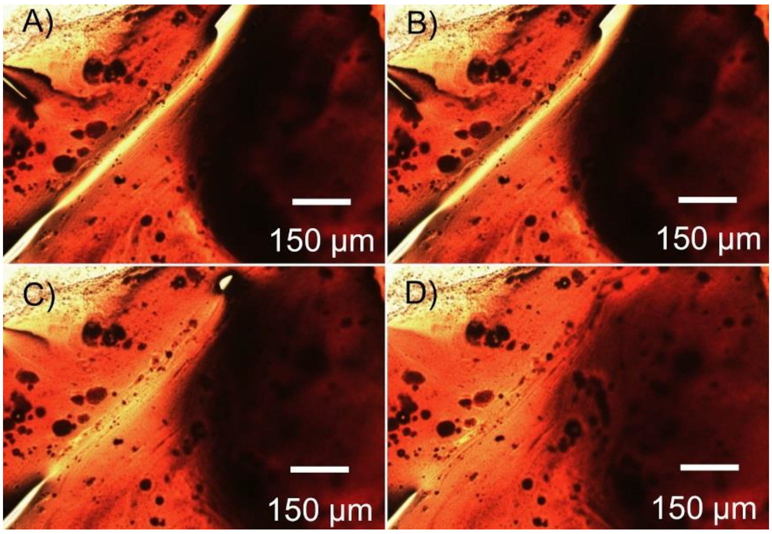

Figure S29. Optical micrographs of film of **3** after defect formation where; A) 0 minutes (20 °C), B) 60 minutes (20 °C), C) heated to 45 °C, D) heated to 50 °C after defect formation (heating rate 2 °C /min) (film thickness = 1 mm).

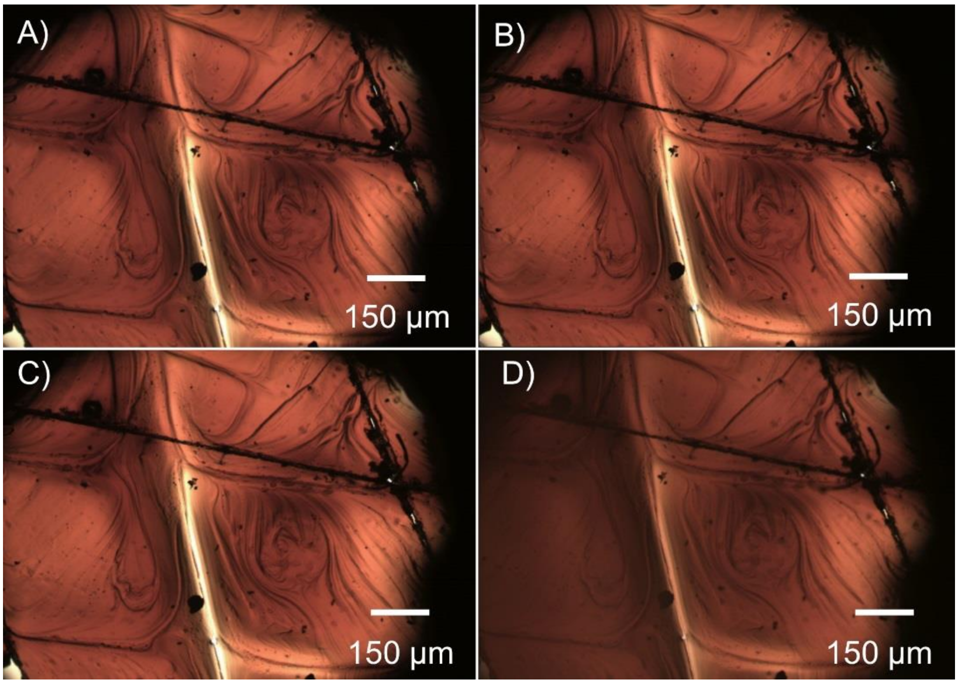

Figure S30. Optical micrographs of film of **1/2** (1:1 % wt) after defect formation where; A) 0 minutes (20 °C), B) 60 minutes (20 °C), C) heated to 100 °C, D) heated to 200 °C after defect formation (heating rate 2 °C /min) (film thickness = 1 mm).

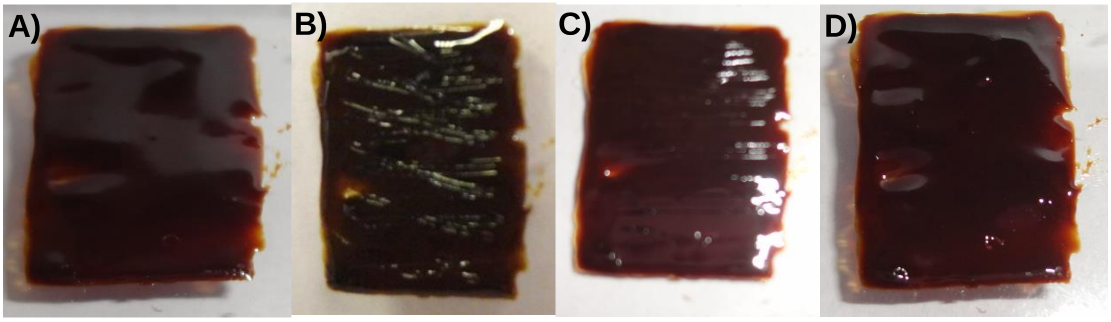

Figure S31. Film of **1**/**3** (1:1 by wt.) where; A) pristine cast film, B) damage (scratches) initiated with scalpel, C) slide after 20 minutes, D) healed sample after 40 minutes (average film dimensions 5 × 9 × 1 mm).

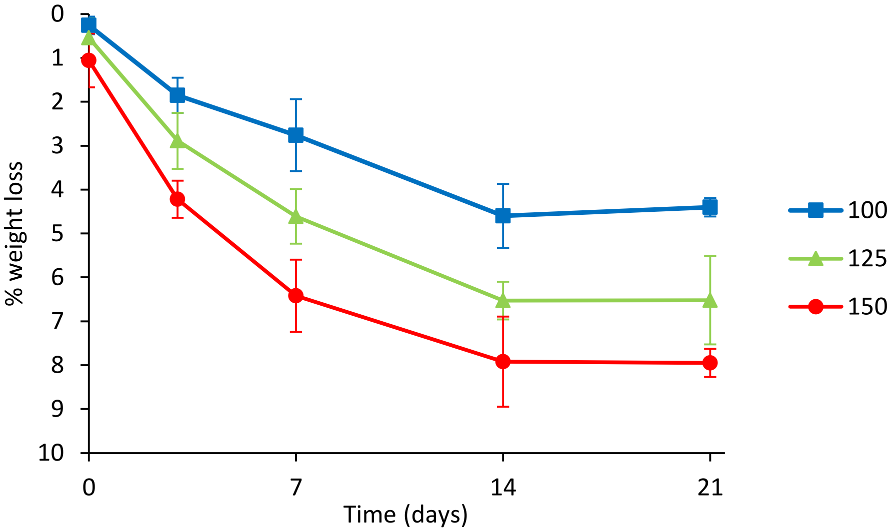

Figure S32. Percentage weight loss (at varying temperatures) from a film of **1** as a function of the time the film had been allowed to equilibrate with atmospheric moisture at ambient temperature, monitored by TGA (heating rate 5 °C/ min).

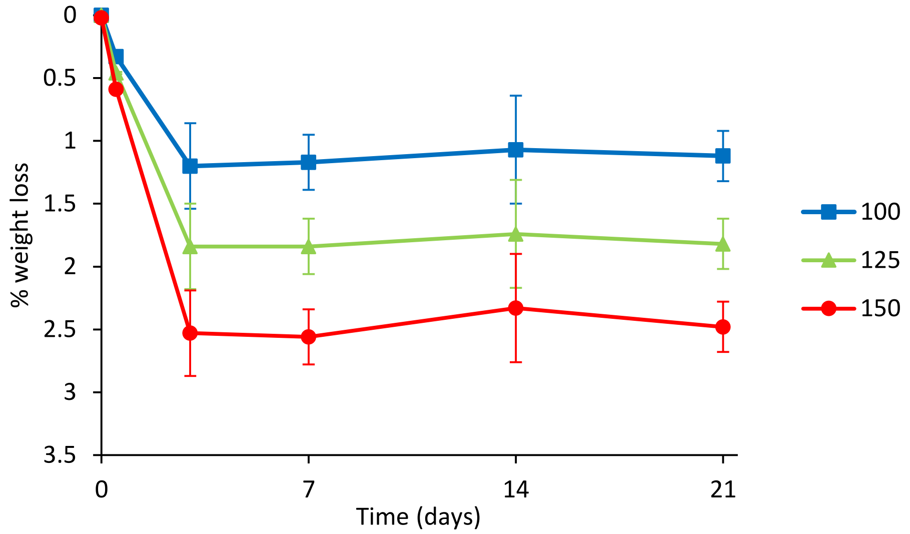

Figure S33. Percentage weight loss (at varying temperatures) from a film of **1/3** (1:1 by wt.) as a function of the time the film had been allowed to equilibrate with atmospheric moisture at ambient temperature, monitored by TGA (heating rate 5 °C/ min).

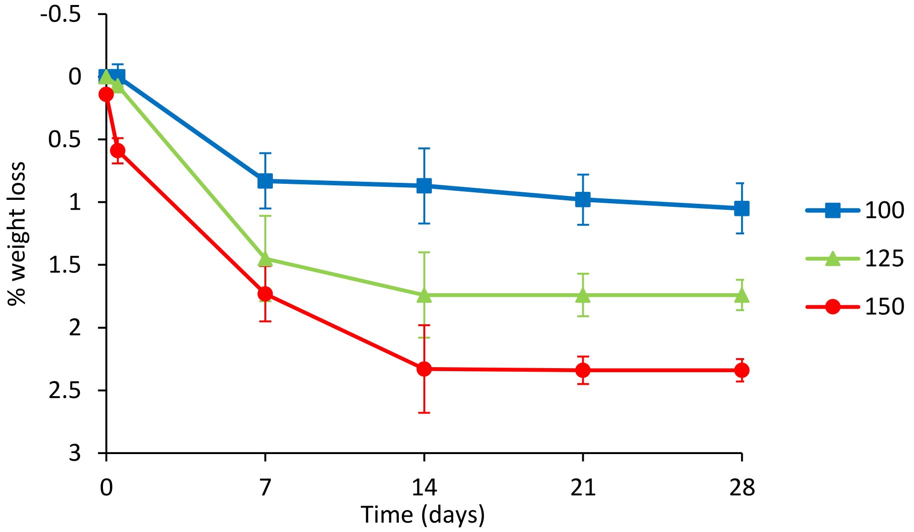

Figure S34. Plot of percentage weight loss (at varying temperatures) from a film of **3** as a function of the time the film had been allowed to equilibrate with atmospheric moisture at ambient temperature, monitored by TGA (heating rate 5 °C/ min).

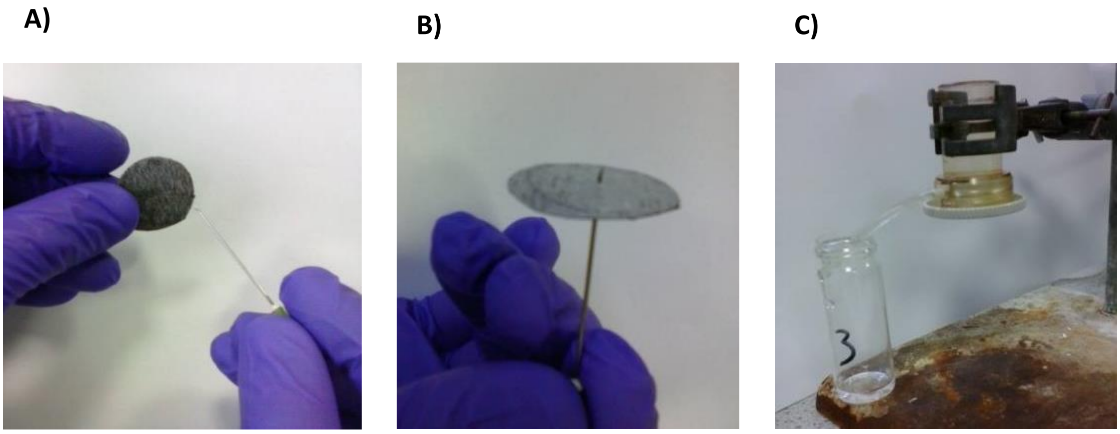

Figure S35. A) Casts of **2/4** (1:1 by wt) between porous paper **B)** defect formation **C)** stirred cell system set up for the study of puncture closure via swelling in water.

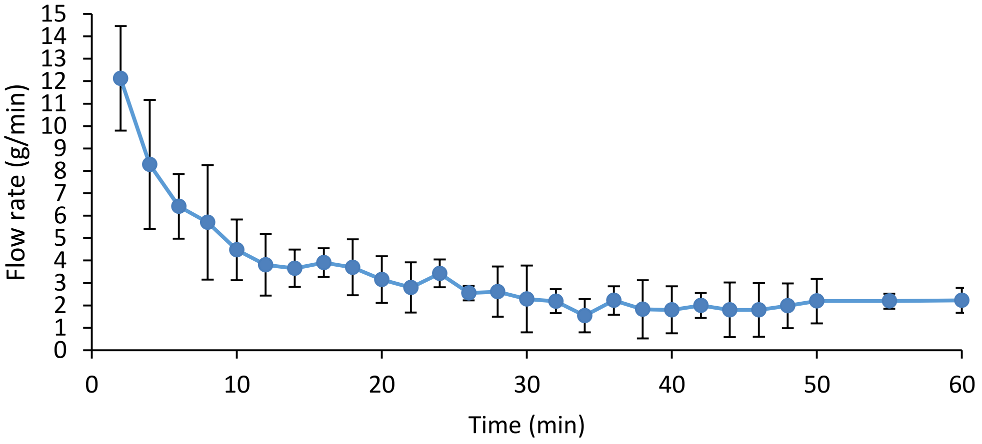

Figure S36. Flow rate of water (under gravity) through a disk of **1** placed between two sheets of porous paper after defects formed via puncture (equivalent to 0.3 % area removal).

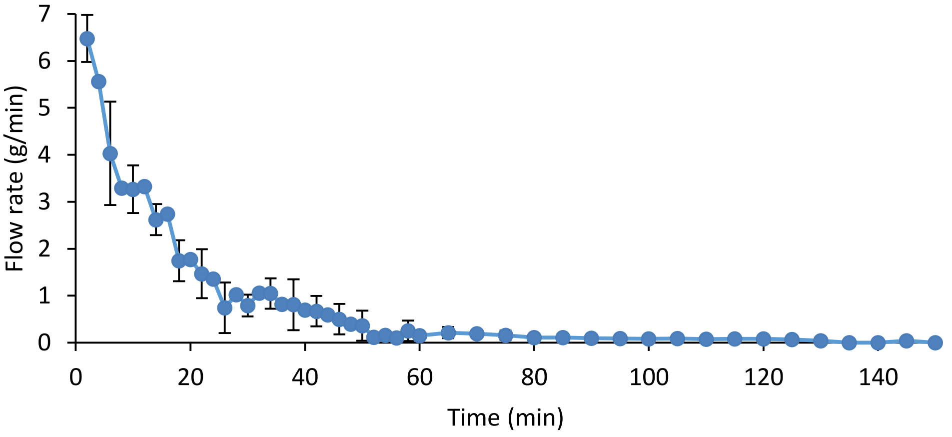

Figure S37. Flow rate of water (under gravity) through a disk **3** placed between two sheets of no-woven PET after defects formed via puncture (equivalent to 0.3 % area removal).

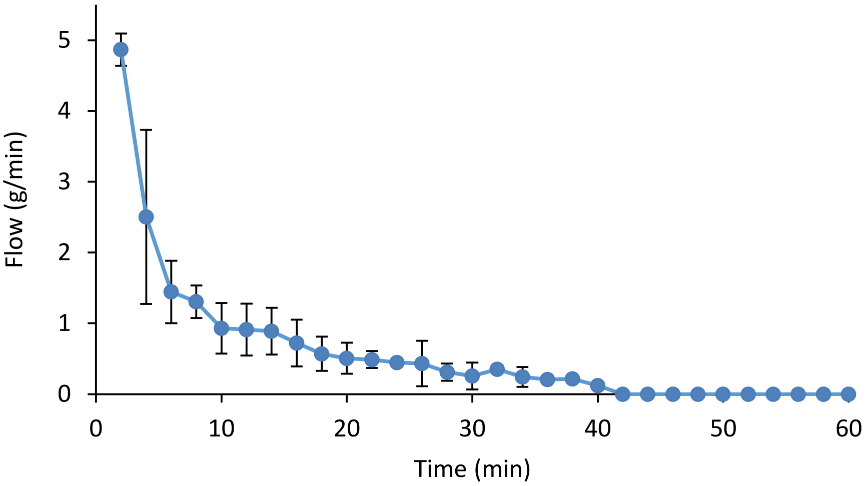

Figure S38. Flow rate of water (under gravity) through a disk of **1/3** (1:1 by wt.) placed between two sheets of non-woven PET after defects formed via puncture (equivalent to 0.3 % area removal).